

Aeroacoustic characterization of acoustically-treated turbulence grids in axisymmetric contraction for open-jet wind tunnels

Quaroni, L.N.; Sinnige, T.; Merino Martinez, R.

DOI

[10.2514/6.2025-3688](https://doi.org/10.2514/6.2025-3688)

Publication date

2025

Document Version

Final published version

Published in

AIAA aviation forum and ASCEND 2025

Citation (APA)

Quaroni, L. N., Sinnige, T., & Merino Martinez, R. (2025). Aeroacoustic characterization of acoustically-treated turbulence grids in axisymmetric contraction for open-jet wind tunnels. In *AIAA aviation forum and ASCEND 2025* Article AIAA 2025-3688 (AIAA Aviation Forum and ASCEND, 2025).
<https://doi.org/10.2514/6.2025-3688>

Important note

To cite this publication, please use the final published version (if applicable).
Please check the document version above.

Copyright

Other than for strictly personal use, it is not permitted to download, forward or distribute the text or part of it, without the consent of the author(s) and/or copyright holder(s), unless the work is under an open content license such as Creative Commons.

Takedown policy

Please contact us and provide details if you believe this document breaches copyrights.
We will remove access to the work immediately and investigate your claim.



Aeroacoustic characterization of acoustically-treated turbulence grids in axisymmetric contraction for open-jet wind tunnels

L. N. Quaroni* and R. Merino-Martínez†

Faculty of Aerospace Engineering, Delft University of Technology, 2629 HS Delft, the Netherlands

The application of an acoustically absorbent material (melamine foam) is investigated for the treatment of turbulence grids in an anechoic open-jet wind tunnel facility featuring an axisymmetric contraction. A comparative study of both the generated turbulence and the grids' self-noise is performed. It is found that the application of melamine foam on the downstream side of the grids marginally affects the produced turbulence, while providing an efficient suppression of tonal peaks in the grids' self-noise spectrum. Broadband noise levels instead show opposing trends depending on the frequency range considered. On the one hand, a general decrease due to the acoustic treatment is observed for Strouhal numbers lower than unity. On the other, an increase, in the form of broad peaks, is seen to occur over certain higher frequency ranges.

List of Symbols

Standard Symbols

A_{flow}	Open area of grids, [m ²]
A_{in}	General nozzle inlet area, [m ²]
A_{out}	General nozzle outlet area, [m ²]
C	Power-law constant of proportionality [-]
d	Bar width, [m]
D_{ext}	Exit diameter of additional axisymmetric contraction, [m]
D_{wt}	Wind tunnel exit diameter, [m]
f_c	Centre frequency [Hz]
K	Kurtosis, [-]
L_p	Sound pressure level referenced to $p_{ref} = 20 \mu\text{Pa}$, [dB – dB/Hz]
L_i	Length of cylindrical melamine foam insert, [m]
$L_{p_{1/12}}$	Sound pressure level of 1/12-octave band centred at f_c and referenced to $p_{ref} = 20 \mu\text{Pa}$, [dB]
M	Mesh width, [m]
r	Radial coordinate, [m]
Re_d	Reynolds number ($= U_\infty d / \nu$), [-]
S	Skewness, [-]
St	Strouhal number ($= fd / U_\infty$), [-]
t_g	Thickness of untreated grids, [m]

*Corresponding author, Postdoctoral researcher, Operations & Environment (O&E), l.n.quaroni@tudelft.nl

† Assistant professor, Operations & Environment (O&E), r.merinomartinez@tudelft.nl

$t_{f,i}$	Thickness of cylindrical melamine foam insert, [m]
t_f	Thickness of grid melamine foam coating, [m]
U	Streamwise velocity at the nozzle exit, [m/s]
u	Streamwise velocity fluctuations, [m/s]
U_∞	Average streamwise velocity at the nozzle exit, [m/s]
u_{rms}	Root-mean-square of streamwise velocity fluctuations, [m/s]
w	Bin width of the normalized histogram, [-]
x	Axial coordinate with origin on downstream plane of turbulence grids, [m]
x'	Axial coordinate with origin at nozzle exit, [m]

Greek Letters

β	Grid porosity ($= A_{flow}/A_{in}$), [%]
γ	Power-law exponent [-]
Λ_x	Longitudinal turbulence integral length scale, [m]
ν	Kinematic viscosity of air at 20°C, [m ² /s]
Φ_{uu}	Power spectrum of streamwise velocity fluctuations, [(m/s) ²]
ϑ	Polar angle of the directivity arc, [°]

Acronyms

CR	Contraction ratio ($= A_{in}/A_{out}$), [-]
HWA	Hot-wire anemometry
LDV	Laser Doppler Velocimetry
OASPL	Overall Sound Pressure Level, [dB(A)]
PDF	Probability density function
SMSB	Square-mesh square-bar
TI	Streamwise turbulence intensity ($= 100 u_{rms}/U_\infty$), [%]

I. Introduction

Awareness of aircraft acoustic emissions and their negative impact on societal well-being has grown steadily over the past few decades [1]. The introduction of Unmanned Aerial Vehicles (UAVs) for commercial and recreational use, starting in the early 2010s, brought the topic to the general public's attention [2]. Field acoustic measurements allow for a global quantification of aircraft noise emissions and provide invaluable information on the highly site-specific interaction of aircraft noise sources and the surrounding environment [3, 4]. However, this same inherent variability of field testing may hinder a clearer understanding of the role that different components play in the generation of noise [5]. The greater control over environmental conditions during aeroacoustic testing in wind tunnels offers, therefore, a valid alternative to field testing if the effect of specific parameters is to be investigated. Open-jet wind tunnels are particularly well suited for aeroacoustic testing due to the possibility of placing the test section within an anechoic plenum to simulate acoustic free-field conditions above a certain cut-off frequency, depending on the room's geometry [6]. This also enables placing the acoustic measurement equipment outside of the flow, to avoid the contamination of the measurements by hydrodynamic pressure fluctuations [7]. The combined use of flow conditioners and exit nozzles with large contraction

ratios (CR) enables spatially homogeneous inflow velocity fields characterized by vanishingly small turbulence levels. The root-mean-square values of the streamwise velocity fluctuations u_{rms} in typical facilities are usually in the order of 0.1% of the value of the set freestream velocity U_∞ [8–10]. This characteristic makes open-jet wind tunnels also ideal for fundamental fluid dynamics studies across a range of disciplines beyond that of aeroacoustics [11]. On the other hand, aerodynamic noise generation is highly influenced by the presence of turbulence, so much so that the second of Lighthill’s seminal papers on the subject contains the word ‘turbulence’ in its title [12]. The typical lack of turbulence in open-jet wind tunnels can, therefore, be a serious issue if the phenomenon under consideration is defined by it. A classic example is the case of turbulence-airfoil interaction, whereby the presence of a fluctuating lift force on a stationary airfoil greatly increases its noise emissions [13]. The large number of propulsive solutions employing propellers in UAVs and other advanced air mobility solutions has also increased the instances of rotor-propeller interaction, with the presence of turbulent inflows to the rotor disk as a common side effect, e.g. [14]. In addition, novel aircraft configurations typically consider propulsive systems featuring boundary layer ingestion for its propulsive advantages [15].

An efficient method for simulating turbulent inflow conditions is to generate nearly-isotropic and nearly-homogeneous turbulence through the use of grids placed perpendicularly to the flow. A slight contraction ($CR \approx 1.3$) immediately downstream of the grid helps in improving the resulting flow isotropy [16]. Roach [17] provided guidelines for the design of such grids in the case of closed-section wind tunnels, whereas Kurian & Fransson [18] offered a complete overview of their characterization through hot-wire anemometry (HWA). However, the lack of confinement in open-jet facilities makes the design of such grids more complicated, with no comprehensive set of guidelines currently available. Due to the increased popularity of open-jet aeroacoustic facilities, though, knowledge on the subject is rapidly increasing. Given the intended applications of these grids, investigations involving their use in open-jet wind tunnels focus on their noise generation properties, as well as on their turbulence production characteristics. Geyer *et al.* [19] measured the pressure losses and the noise generation induced by flow through fine screens and nets at the nozzle exit of an open-jet wind tunnel. It was reported that, for such types of flow conditioners, the dominant noise source at low frequencies was the wind tunnel jet itself, whereas the net parameters became increasingly more important at higher frequencies. Bowen *et al.* [20] focused on single-plane grids with relatively large square mesh sizes more typical of previous aeroacoustic studies involving the use of turbulence grids, e.g. [21, 22]. They produced a comprehensive dataset of both noise emissions and turbulence statistics generated by grids with different mesh sizes and different contraction ratios, with particular emphasis on the possible benefits arising from the additional contraction downstream of the grid. This last part was achieved by placing the grids at different positions along the wind tunnel’s fixed converging nozzle. They showed that a contraction ratio $CR \approx 4$ produced turbulence characteristics comparable with the suggested $CR \approx 1.3$ for improved isotropy, with the added benefit of a considerable reduction in the grids’ self-noise. More recently, Li *et al.* [23] complemented previous works ([24, 25]) on the possible benefits of adding acoustic-absorbent material on the downstream side of turbulence grids to reduce the grids’ self-noise. The addition of the acoustic absorbing material had a limited effect on the generated turbulence statistics, with slight improvements in self-noise mitigation over certain frequencies and increased self-noise levels over others. A major advantage of the acoustic treatment was the suppression of tones that were related to vortex shedding near the grids. The same issue (vortex-shedding tonal noise) was also observed under certain conditions by Bowen *et al.* [20].

It is worth noting that all the work cited above deals with open-jet contractions of rectangular cross-sections. The present contribution is, therefore, meant as an extension of these investigations to the case of axisymmetric nozzles, whose symmetry might prove beneficial in certain applications where axial symmetry is preferred (i.e. propeller studies). In particular, the case of square-mesh arrays of square bars (SMSB) grids with and without the application of acoustic absorbing material on the downstream side and placed upstream of a slight contraction ($CR \approx 2$) is considered. The remainder of the paper is structured as follows. Section II outlines the experimental setup employed and the test conditions. Section III presents the results in terms of the characteristics of the generated turbulence and the corresponding self-noise levels. Finally, Section IV draws some conclusions.

II. Experimental setup and test conditions

A. Overview

The experiments were conducted at the vertical, open-jet, anechoic wind tunnel (‘A-Tunnel’) of Delft University of Technology. The main characteristics of the facility can be found in the work by Merino-Martínez *et al.* [26]. The setup

consists of an axisymmetric contraction mounted at the exit of the main wind tunnel’s circular nozzle ($D_{wt} = 600$ mm) and of three single-plane SMSB grids which can be inserted between the main wind tunnel exit and the additional contraction (see Figs. 1 and 2). The axisymmetric contraction was 3D-printed, whereas the grids were produced through water-jet cutting of 5-mm-thick (t_g) aluminum sheets. The contraction ($CR \approx 2$, $D_{ext} = 420$ mm) was added in an effort to both improve the turbulence isotropy, increase the maximum attainable flow velocity, and mitigate the self-noise generation of the grids, as suggested by Bowen *et al.* [20].

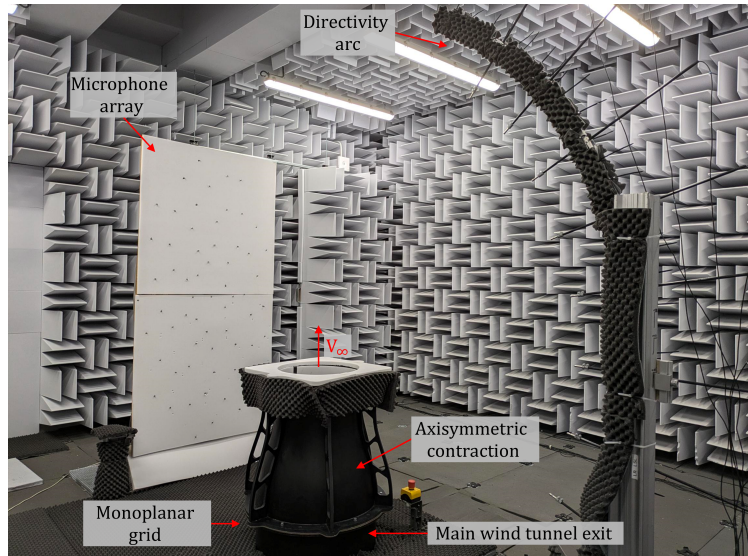


Fig. 1 Overview of the experimental setup during acoustic testing at the open-jet anechoic wind tunnel (‘A-Tunnel’) of Delft University of Technology. Note the melamine foam panel covering the 64-microphone array.

Both contraction and grids were developed and utilized for the investigation of the acoustic emissions by an isolated propeller subjected to turbulent inflow, as detailed in Quaroni *et al.* [27]. The data presented here for the untreated grids were collected during that experimental campaign and served as a reference for the propeller measurements. Nevertheless, acoustic reflections and strong tonal peaks were found to contaminate the acoustic data [28]. In a subsequent test campaign, a series of preventive measures were taken. In particular, pyramidal polyurethane foam and melamine foam panels were applied to all exposed surfaces, including the nozzle flange, see Figure 1. Additionally, a 10-mm thick melamine foam sheet with a 10° -slope leading edge was placed around the inner walls of the contraction’s end cylindrical section of length $L_i = 150$ mm, see Fig. 2. Additional information regarding the foam treatments of the nozzle can be found in [28]. Drawing from the work of Li *et al.* [23], melamine foam panels of thickness t_f equal to 20 mm were water-jet cut and applied downstream of the grids to both mitigate acoustic reflections coming from downstream and prevent the generation of vortex-shedding tones.

Table 1 Geometric parameters of turbulence grids (see the List of Symbols and Figure 2 for the definition of each parameter).

Grid	β	d	M	t_g	M/D_{wt}	d/M	t_g/M
[-]	[%]	[mm]	[mm]	[mm]	[-]	[-]	[-]
A	64	7	35	5	0.06	0.20	0.14
B	64	10	50	5	0.08	0.20	0.10
C	64	12	60	5	0.10	0.20	0.08

Figure 2 depicts a cross-sectional view of the axisymmetric contraction and the design parameters characterizing the grids (i.e. bar width d and mesh width M) while Table 1 lists their values. The design of the grids was based on the

limits of $\beta \geq 50\%$ and $M/D_{wt} \leq 0.1$ for reducing the risk of flow instabilities and the inhibition of the generated turbulence by interaction with the inner walls of the contraction as reported by Roach [17].

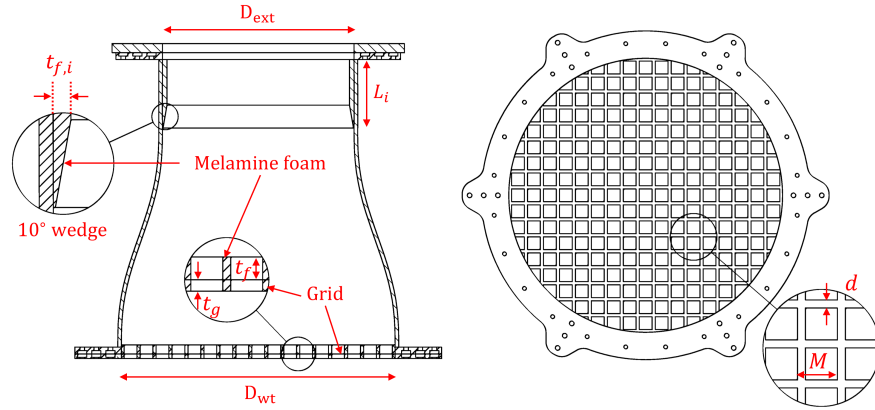


Fig. 2 Cross-sectional view of the axisymmetric contraction, detailing the positions of the melamine foam inserts (left) and schematic view of the design parameters identifying the square-mesh turbulence grids geometry (right). Note that the melamine foam inserts on the contraction are not present in the case of the ‘clean’ untreated grids.

B. Measurement techniques

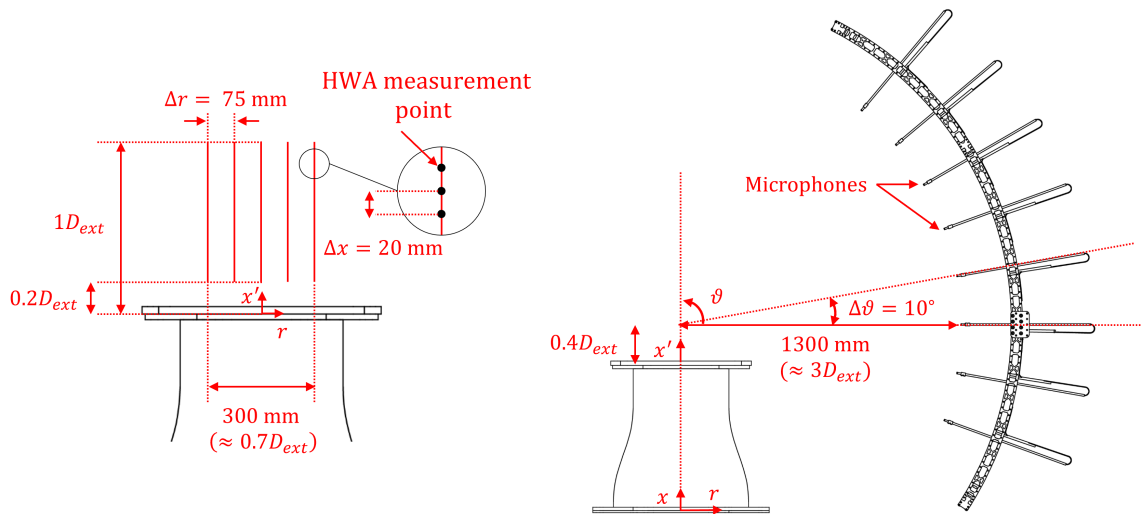


Fig. 3 Illustration of the hot-wire measurement grid (left) and positioning of the 8-microphone directivity arc with respect to the axisymmetric contraction (right).

HWA was used to quantify the turbulence-producing properties of the system composed of the contraction and the grids. In particular, a single-wire probe (*Dantec 55P11*) recorded the time series of the streamwise velocity U at different

planes between $0.2 D_{ext}$ and $1 D_{ext}$ downstream of the nozzle exit, with steps $\Delta x = 20$ mm. This was done for five different radial positions ($\Delta r = 75$ mm) starting from the contraction's axis in order to characterize the flow homogeneity (see Fig. 3, left). The cases of contraction-only (i.e., no grids) were also measured to serve as a reference. For each measurement point, the recording time was 15 s with a sampling frequency of 51,200 Hz. Acoustic measurements were performed using a 64-microphone array and an 8-microphone directivity arc for source directivity analysis. Both microphone arrays were placed at a distance of 1300 mm ($\approx 3 D_{ext}$) from the nozzle's symmetry axis. The directivity arc spans an angle of 70° with microphones distanced at steps of $\Delta\theta = 10^\circ$ from each other, and it is centred at a point $0.4 D_{ext}$ above the centre of the nozzle's outlet, as shown in Figure 3 (right). This choice was based on the position of the propeller's disk during the campaign detailed in [27]. Microphone signals were acquired for a total of 60 s per test condition, also at a sampling frequency of 51,200 Hz.

C. Test conditions

Turbulence characterization was performed for two inflow velocities U_∞ of 20 m/s and 30 m/s. Additionally, the case with untreated grids was also tested at 40 m/s, and the case with acoustically-treated grids and nozzle at 25 m/s. This difference is due to an adjustment in the test conditions for the main experiment involving a turbulence-ingesting propeller. This was operated with U_∞ equal to 25 m/s and 30 m/s both in the campaign detailed in [27] and in the subsequent one reported in [29]. Acoustic measurements were instead performed for a velocity sweep from 5 m/s to 60 m/s with 5 m/s step increments for all 'clean', untreated grid cases, and from 10 m/s to 40 m/s with 5 m/s step increments for the acoustically-treated cases. The difference is again due to adjustments in the test conditions for the two campaigns involving the propeller.

III. Results

The present section is subdivided into two subsections. In particular, III.A reports the comparison between the turbulence properties generated by the sets of grids with and without acoustic treatment; III.B deals instead with the comparison of their self-noise generation.

A. Characteristics of the generated turbulence

The main purpose of the grids is to produce nearly-isotropic and homogeneous turbulence for aeroacoustic investigations. A complete analysis of the isotropy of turbulence would require the measurement of the pointwise velocity fluctuation vector \mathbf{v} , obtainable through e.g. HWA with cross-wire/triple-wire probes. Single-wire probes are mainly sensitive to the velocity component perpendicular to the length of the wire, which corresponds to the primary streamwise velocity U . Knowledge of only the streamwise velocity fluctuations u allows, nonetheless, to make some considerations on the state of the generated turbulence by comparison with the well-known statistical properties of canonical freely-decaying turbulence.

1. Downstream evolution

The evolution of both turbulence intensity and longitudinal integral length scale downstream of the grids is first discussed. The (streamwise) turbulence intensity TI is computed as:

$$TI = \frac{u_{\text{rms}}}{U_\infty}, \quad \text{where} \quad u_{\text{rms}} = \sqrt{\frac{1}{N} \sum_{j=1}^N u_j^2}, \quad (1)$$

with N being the total number of samples and u_j the j -th value in the time series of the streamwise velocity fluctuation u . The longitudinal integral length scale Λ_x is determined through the temporal autocorrelation function R_{uu} :

$$\Lambda_x = U_\infty \int_0^{+\infty} R_{uu}(\tau) d\tau, \quad \text{with} \quad R_{uu}(\tau) = \lim_{T \rightarrow \infty} \frac{1}{T} \int_0^T u(t) \cdot u(t + \tau) dt, \quad (2)$$

where use has been made of Taylor's frozen turbulence hypothesis to transfer the correlation from the spatial domain to the temporal domain [30]. In a discrete form, (2) has the following expression:

$$\Lambda_x = U_\infty \Delta t \sum_{j=1}^{N^*} R_{uu}^{(j)}, \quad \text{with} \quad R_{uu}^{(j)} = \left(\sum_{k=0}^{N-j-1} u_{k+j} \cdot u_k \right) \cdot \left(\sum_{k=0}^{N-1} u_k^2 \right)^{-1}, \quad (3)$$

where the sample $N^* + 1$ corresponds to the sample for which $R_{uu}^{(j)}$ reaches its first zero crossing [31]. Figure 4 reports the downstream evolution of TI and the relative difference $\Delta TI = (TI_{\text{foam}} - TI_{\text{clean}})/TI_{\text{clean}}$ for all tested configurations (centreline $r/D_{\text{ext}} = 0$, $U_\infty = 30$ m/s). It can be seen that turbulence levels monotonically decrease with increasing distance from the grids, as expected from freely-decaying turbulence [32]. Expressing the streamwise distance x between the grids and the hot-wire measurement point in terms of grid bar widths (i.e. x/d) allows further considerations. In particular, the differences in the observed turbulence levels between grids can be partly explained by the lower value of x/d for increasing values of the bar width d for a constant axial coordinate x . The curves, however, do not perfectly collapse, indicating additional effects. Coincidentally, the curve for the coarsest grid (grid C) after acoustic treatment agrees with the curves for the intermediate grid (grid B). Addition of melamine foam leads to a slight decrease in turbulence intensity over the studied x/d range for all grid sizes, especially for the finest and the coarsest grids A ($\approx 4\%$ less than its ‘clean’ version) and C ($\approx 6\%$ less). This is in agreement with the findings of Li *et al.* [23].

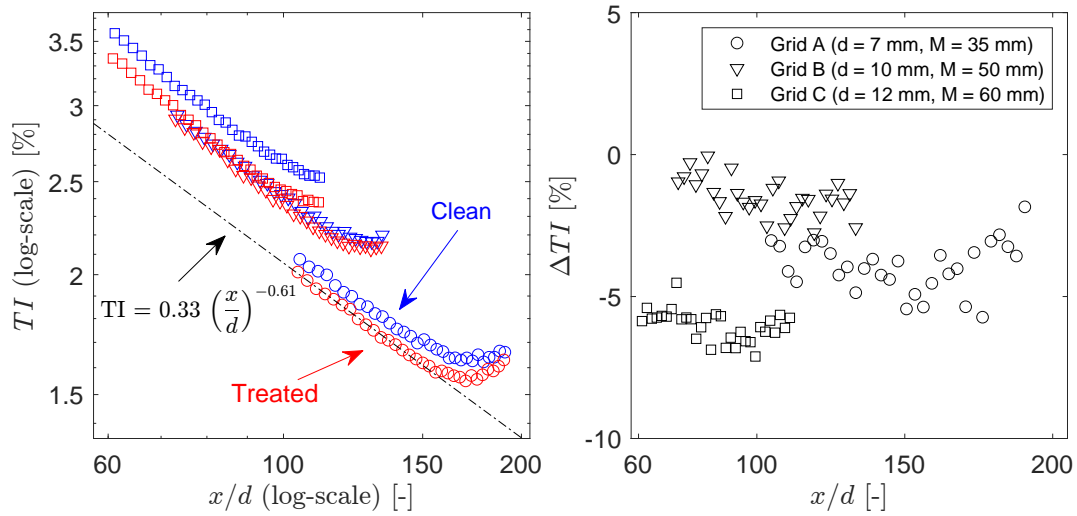


Fig. 4 Streamwise evolution of turbulence intensity TI (left) and relative difference $\Delta TI = 100 (TI_{\text{foam}} - TI_{\text{clean}})/TI_{\text{clean}}$ (right) for all grids with and without acoustic treatment along the contraction’s axis ($r/D_{\text{ext}} = 0$) and with a constant exit velocity $U_\infty = 30$ m/s. The power-law curve fit (dashed line, left plot) is shown only for treated grid A for improved readability. The origin of the axial coordinate x is on the grids’ downstream plane.

Table 2 Estimate of parameters from Equation (4) through least-square fitting of the experimental data shown in Figure 4.

Grid		γ	C
		[-]	[-]
A	Clean	-0.60	0.34
	Treated	-0.61	0.33
B	Clean	-0.62	0.46
	Treated	-0.64	0.46
C	Clean	-0.66	0.55
	Treated	-0.68	0.55

Roach [17] argued that the streamwise evolution of the turbulence intensity TI can be expressed in the form of a power law:

$$TI = C \left(\frac{x}{d} \right)^\gamma \quad (4)$$

with the constants $C = 1.13$ and $\gamma = -0.71$ derived from an extensive dataset of closed-section wind tunnel experiments. The logarithmic plot in Figure 4 (left) confirms such a trend over most of the measurement distances for all grid cases. Deviations are present at the higher end of x/d , when the turbulence intensity tends to plateau (grids B and C) or slightly increase (grid A). Fitting the curve given by (4) to the data points falling outside of this deviation range in the least-squares sense allows the estimation of the two parameters C and γ . The current experimental results (Table 2) show values which are in the same order of magnitude as those obtained by Roach ([17]), even though lower for C and higher for γ in all grid cases. These differences could derive from the lack of confinement in the current setup (open-jet) and the presence of the contraction immediately downstream of the grids. Figure 4 (left) reports the resulting curve fit for the case of grid A (treated) as an example.

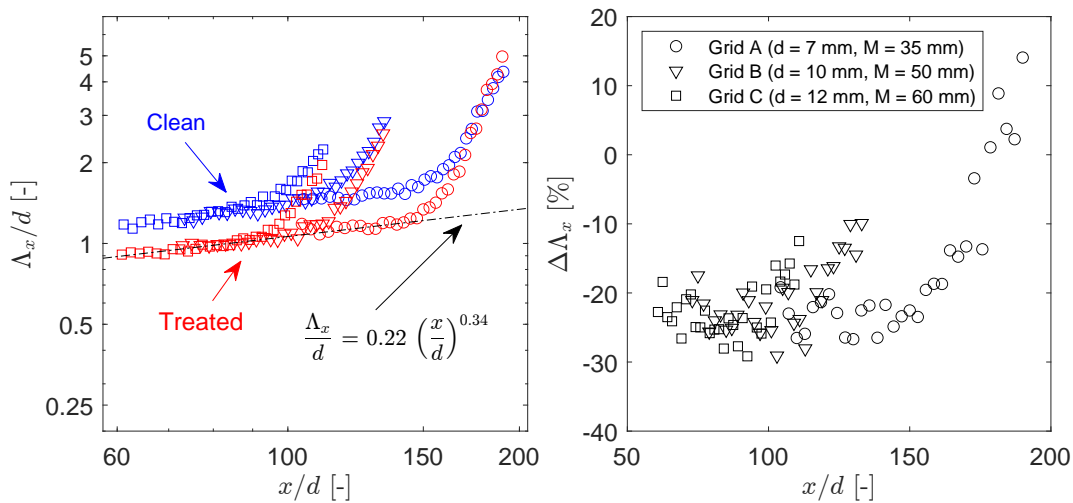


Fig. 5 Streamwise evolution of longitudinal integral length scale Λ_x (left) and the relative difference $\Delta\Lambda_x = (\Lambda_{x_{\text{foam}}} - \Lambda_{x_{\text{clean}}})/\Lambda_{x_{\text{clean}}}$ (right) for all grids with and without acoustic treatment along the flow contraction's centreline ($r/D_{\text{ext}} = 0$) and with a constant exit velocity $U_\infty = 30$ m/s. Power-law curve fit (dashed line, left plot) shown only for treated grid A for improved readability. The origin of the axial coordinate x is at the grids' downstream plane.

Figure 5 reports the streamwise evolution of the longitudinal integral length scale Λ_x (normalized by the grid bar width d) along the contraction's centreline for the same conditions as for Figure 4. The collapse between the curves for different mesh dimensions is evident for both 'treated' and 'clean' grids. As with the turbulence intensity, the application of melamine foam leads to an overall decrease in the longitudinal integral length scale when compared to the corresponding 'clean' case. This is again in agreement with the study of Li *et al.* [23], though the magnitude of the decrease ($\approx 25\%$ with respect to the 'clean' case) is larger than that observed in their work ($\approx 10\%$). The overall trend can also be represented through a power law of the same form as (4). As an example, Fig. 5 (left) shows the curve obtained from fitting the data for the 'treated' grid A in the range outside of the deviation from linearity (in a logarithmic sense), leading to the estimates $C = 0.22$ and $\gamma = 0.34$. The deviation from the power law occurs at roughly the same non-dimensional distance x/d as that in the turbulence intensity, suggesting a common effect. In this respect, further insights can be gained if the distance x of the hot-wire measurement point from the grid is substituted with the distance x' from the nozzle exit, normalized by the nozzle exit diameter D_{ext} . Figure 6 shows how for $1 \leq x'/D_{\text{ext}} \leq 1.4$ the turbulence intensity reaches a plateau and the (normalized) longitudinal integral length scale has a dramatic upward shift in all of the grids (shown here only for the treated cases). In general, the finer the grid, the sooner this 'transition' seems to occur. A similar trend was also observed for a rectangular nozzle and untreated grids in the study by Bowen *et al.* [20].

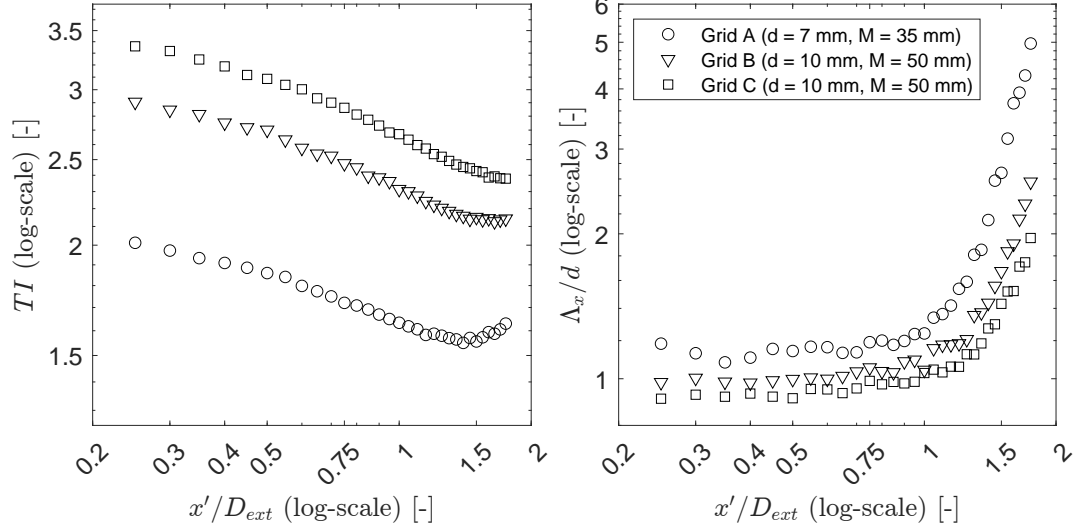


Fig. 6 Streamwise evolution of turbulence intensity TI (left) and normalized longitudinal integral length scale Λ_x/d (right) for all acoustically-treated grids along the flow contraction's centreline ($r/D_{ext} = 0$) and with a constant exit velocity $U_\infty = 30$ m/s. The origin of the axial coordinate x' is at the nozzle exit.

Figure 7 reports the evolution of the turbulence intensity and the integral length scale along measurement lines at different radial locations (see Figure 2, left) for the case of the acoustically-treated grid C (similar trends were obtained for the other cases). It can be seen how the contraction is characterized by a good homogeneity of the turbulence characteristics across the considered radial range until $x'/D_{ext} \approx 0.65$, after which the two outermost lines with respect to the axis of the contraction ($r'/D_{ext} = \pm 0.35$) show an abrupt increase in turbulence intensity and integral length scale. The large differences observed between the two radially symmetric lines starting from $x'/D_{ext} > 0.9$ could be attributed to a combination of vibration disturbances (larger intrusion of the HWA probe-holder into the flow for $r/D_{ext} = 0.35$) and hot-wire positioning uncertainties.

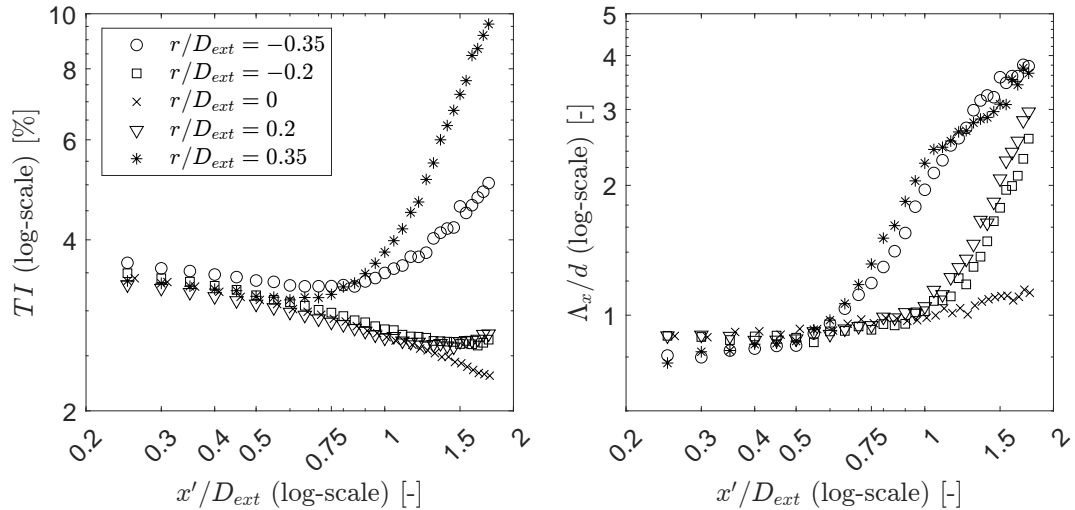


Fig. 7 Streamwise evolution of turbulence intensity TI (left) and normalized longitudinal integral length scale Λ_x/d (right) for the acoustically-treated grid C along measurement lines at different radial locations (Figure 2) with a constant exit velocity $U_\infty = 30$ m/s. The origin of the axial coordinate x' is at the nozzle exit.

The two ‘intermediate’ lines ($r'/D_{ext} = \pm 0.2$) instead show this deviation further downstream, at around $x'/D_{ext} \approx 1.2$, while the contraction's symmetry line is only slightly affected at the very end of the axial range of measurement. This points to the involvement of the open-jet shear layer, whose influence is spreading inwards for increasing axial distances

from the nozzle exit. Similar trends were obtained for the other grids, with the only difference being an earlier onset of the deviation along x'/D_{ext} the finer the tested mesh. No noticeable differences were observed between the ‘clean’ and the acoustically-treated cases. Finally, Figure 8 shows an almost perfect collapse of the trends of the turbulence intensity TI and the integral length scale Λ_x along the contraction symmetry line for three inflow velocities U_∞ (20, 25, and 30 m/s) for the same treated grid C, highlighting the independence of the two quantities from U_∞ in this range.

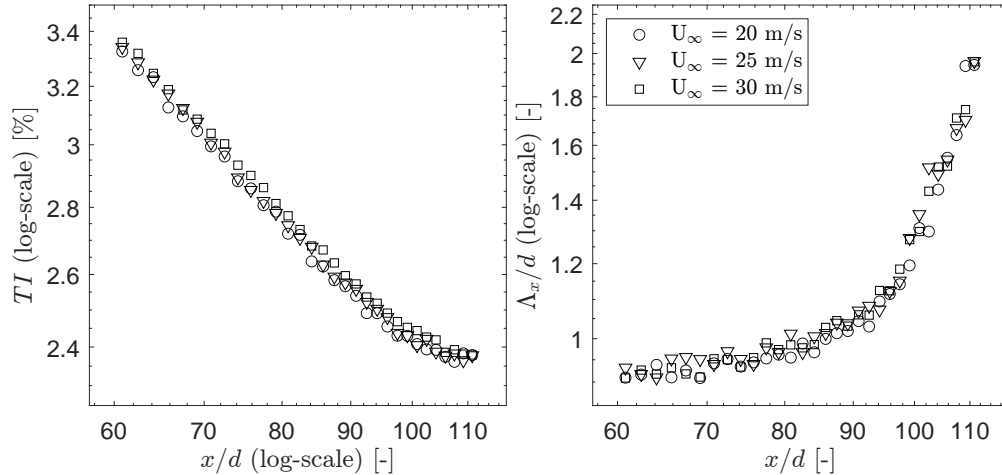


Fig. 8 Streamwise evolution of turbulence intensity TI (left) and normalized longitudinal integral length scale Λ_x/d (right) for acoustically-treated grid C along the contraction symmetry line for three inflow velocities.

2. Higher-order statistics

Truly isotropic turbulence is a stationary stochastic Gaussian process, i.e., the probability distribution function (PDF) of the inflow velocity follows a Gaussian curve and its statistical moments are independent of time. Figure 9 shows the histograms of the normalized velocity U/U_∞ and a normal distribution with the same mean and standard deviation as the experimental data for the acoustically-treated grid C with $U_\infty = 30$ m/s at two different positions. ‘Point 1’ lies in the open jet’s core along the symmetry axis of the contraction at $x'/D_{ext} = 0.4$ while ‘Point 2’ lies at $x'/D_{ext} = 1.6$ at the outermost radial position considered $r/D_{ext} = 0.35$, in a region highly affected by the open jet’s shear layer (see the discussion in III.A.1).

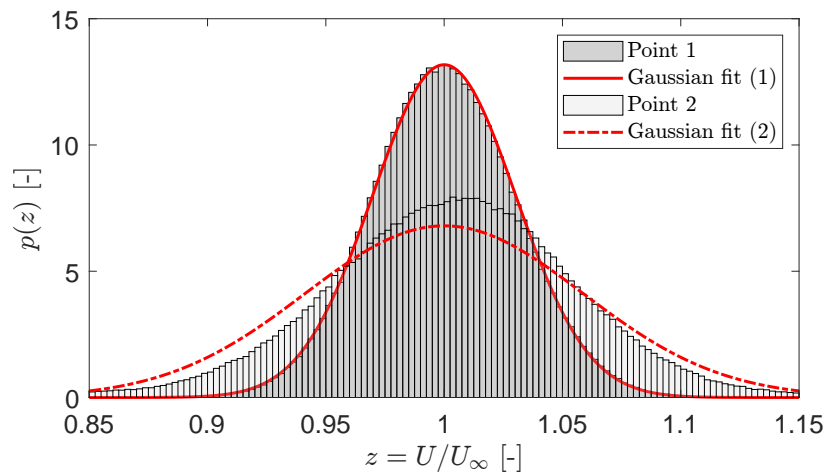


Fig. 9 Normalized histograms of $z = U/U_\infty$ at points ($r/D_{ext} = 0, x'/D_{ext} = 0.6$) and ($r/D_{ext} = 0.35, x'/D_{ext} = 1.6$) for the case of the acoustically-treated grid C and $U_\infty = 30$ m/s (bin width $w = 0.0025$). Normal distributions (mean and standard deviations of the recorded time series at the two points) are highlighted in red.

The normalized histograms of the experimental data are computed as:

$$p(z_j) = \frac{N_j}{N \cdot w} \quad (5)$$

where N_j is the number of occurrences of $z = U/U_\infty$ which fall within the j -th bin, centred around z_j , of a given bin width w . It is clear how the normal distribution properly captures the experimental one of U/U_∞ at ‘Point 1’, while it results in a poorer fit in the case of ‘Point 2’. This highlights the effect of both increasing the distance from the grids and the open jet’s shear layer in modifying the turbulence statistics.

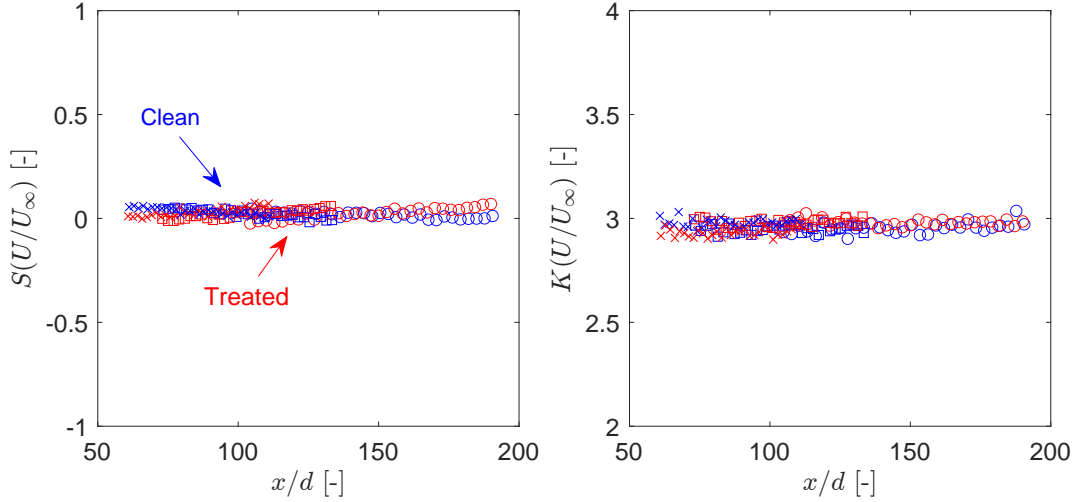


Fig. 10 Streamwise evolution of skewness S (left) and kurtosis K (right) of U/U_∞ for ‘clean’ and acoustically-treated grids along the contraction symmetry line for $U_\infty = 30$ m/s. The origin of the axial coordinate x is on the grids’ downstream plane.

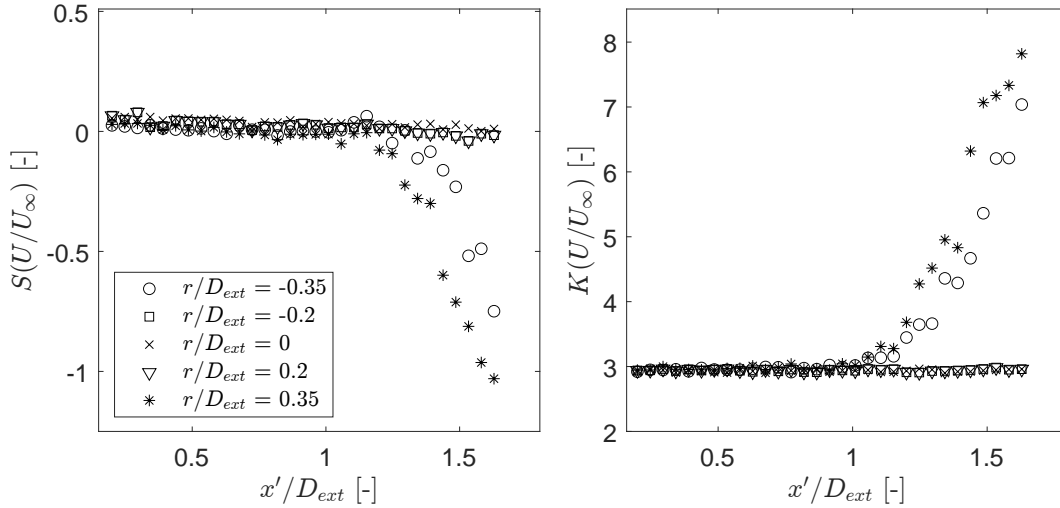


Fig. 11 Streamwise evolution of skewness S (left) and kurtosis K (right) of U/U_∞ for acoustically-treated grid C along measurement lines at different radial locations (Figure 2) with a constant exit velocity $U_\infty = 30$ m/s. The origin of the axial coordinate x' is at the nozzle exit.

A convenient way to assess the quality of a Gaussian fit to the experimentally determined distributions is by employing the statistical descriptors of skewness S and kurtosis K [20, 23, 33]. These are defined as:

$$S = \frac{1}{N} \sum_{j=1}^N \left(\frac{x_j - \bar{x}}{s} \right)^3 \quad \text{and} \quad K = \frac{1}{N} \sum_{j=1}^N \left(\frac{x_j - \bar{x}}{s} \right)^4, \quad (6)$$

where \bar{x} is the mean of the time series and s is its standard deviation. The skewness S is a measure of the asymmetry of the distribution with respect to the mean of a time series, whereas the kurtosis K is a measure of its ‘flatness’. A Gaussian distribution yields $S = 0$ and $K = 3$, and a comparison of the trends of these two quantities with these values can be an effective method to test for the normality of the velocity fluctuations. Figure 10 reports the trends of S and K for the ‘clean’ and treated grids along the contraction’s symmetry line, showing how the Gaussian hypothesis is valid over the whole measurement distance in both cases. The effect of the shear layer in ‘distorting’ the distribution of U/U_∞ is clearly seen if the values of S and K are reported for the other radial strips considered and the streamwise distance is represented by x'/D_{ext} (Figure 11).

3. Spectral characteristics

Turbulence is an inherently three-dimensional process and, in a homogeneous and isotropic field, the fluctuations are not directed towards any particular direction. The semi-empirical fit by von Kármán describes how the total kinetic energy coming from all possible directions is distributed over different scales [34]. If Taylor’s ‘frozen turbulence’ hypothesis is valid, the velocity fluctuations measured at a fixed point in space (e.g., through HWA) can be related to the turbulent velocity field being convected with velocity U_∞ and passing through the same fixed point [35]. A common engineering approximation for the energy spectrum that would be observed in this case is given by:

$$\Phi_{uu}(\text{St}) = \frac{4\overline{u^2}\Lambda_x}{U_\infty} \frac{1}{\left[1 + \left(\frac{k_x}{k_e} \right)^2 \right]^{5/6}}, \quad (7)$$

with:

$$\text{St} = \frac{f\Lambda_x}{U_\infty} \quad \text{and} \quad \frac{k_x}{k_e} = 2\sqrt{\pi} \frac{\Gamma(5/6)}{\Gamma(1/3)} \text{St}, \quad (8)$$

where St is the Strouhal number based on the longitudinal integral length scale Λ_x and the streamwise average flow velocity U_∞ , Γ is the Gamma distribution, k_x is the longitudinal wavenumber, and k_e is the wavenumber range of the energy-carrying eddies [20].

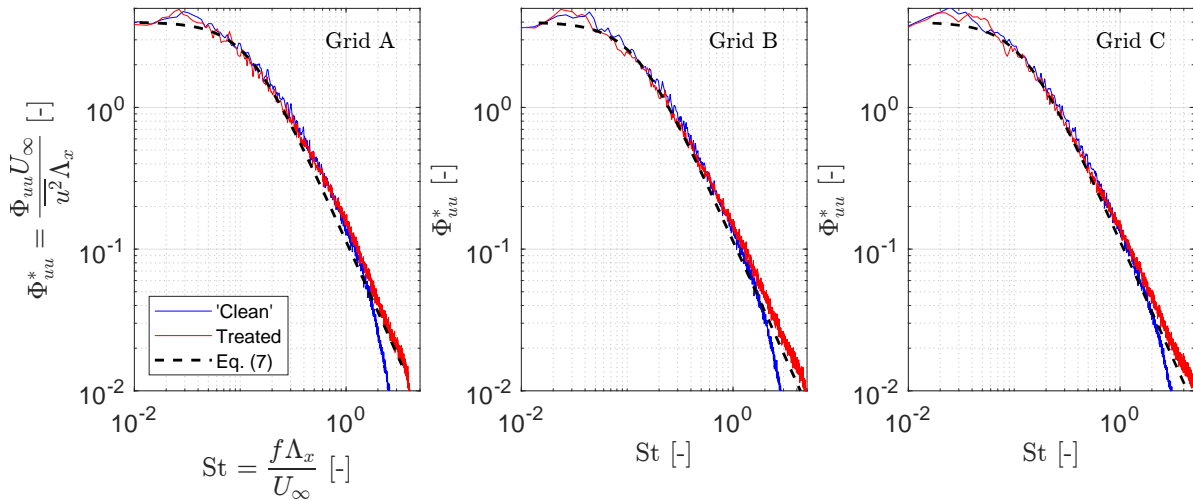


Fig. 12 Normalized power spectra of the streamwise velocity fluctuations u for ‘clean’ and acoustically-treated grids at $(x'/D_{ext} = 0.6, r/D_{ext} = 0)$. The fitted semi-empirical spectrum from (7) is also reported (dashed line). Frequency resolution $\Delta f = 5\text{Hz}$.

The normalized power spectra Φ_{uu}^* of the streamwise velocity fluctuations u for ‘clean’ and acoustically-treated grids at $(x'/D_{ext} = 0.6, r/D_{ext} = 0)$ are reported in Figure 12 together with the curves resulting from the application of (7). For this last part, the longitudinal integral length scale was estimated by means of least-squares fitting (7) to the experimental data. This method yielded slightly larger values of Λ_x than those obtained through application of the temporal autocorrelation in (3). A similar observation was also made by Bowen *et al.* [20]. Both clean and treated grids show very good agreement with the semi-empirical von Kármán formula (7). This, however, does not necessarily imply that the grid-generated turbulence is homogeneous and isotropic, but only that the fit given by (7) is able to reproduce the shape of the velocity fluctuation spectra [35]. One last observation can be made with respect to the fact that the addition of foam seems to ‘delay’ the deviation of the experimental spectra from the von Kármán fit to higher Strouhal numbers. However, this difference might also be caused by the fact that the two datasets (‘clean’ and treated grids) were acquired in different campaigns and using different probes, possibly leading to installation effects.

B. Comparison of self-noise production

The present subsection deals with the comparison of the noise signatures of the different grids, with a particular emphasis on the possible improvements observed through application of the melamine foam treatment.

1. Spectral characteristics

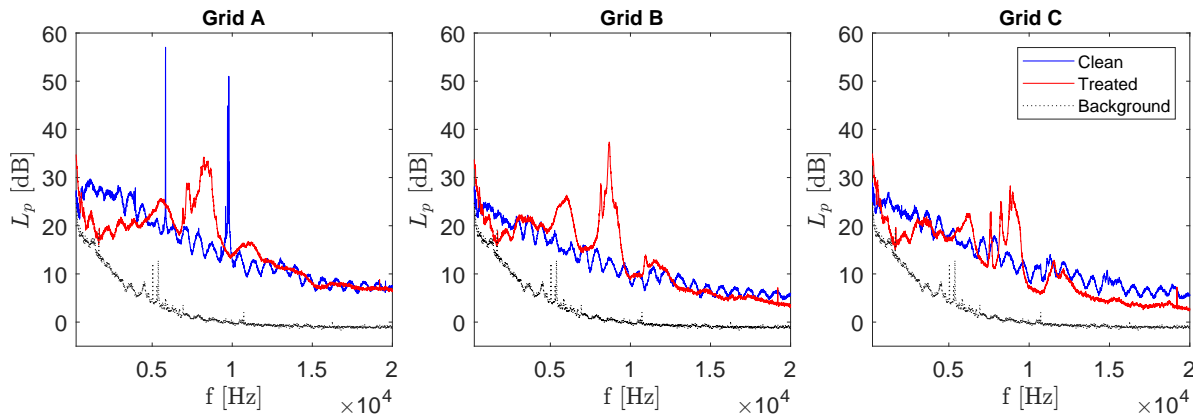


Fig. 13 Comparison of sound pressure level L_p spectra produced by clean and acoustically-treated grids for $U_\infty = 30$ m/s as recorded by a microphone at $\vartheta = 50^\circ$ (scheme in Figure 3, right). Frequency resolution $\Delta f = 5$ Hz.

Figures 13 and 14 report a comparison of the sound pressure level L_p spectra for all grids, both clean and acoustically-treated for a microphone at $\vartheta = 50^\circ$ (scheme in Figure 3, right) and with an inflow velocity $U_\infty = 30$ m/s. This position is chosen as it corresponds to the maximum sound pressure levels recorded along the microphone directivity arc due to the dipole-like radiation pattern exhibited by the grids, see III.B.3. The oscillations observed in the spectra of the clean grids were caused by the presence of spurious acoustic reflections, partly mitigated by the acoustic treatment of the nozzle itself (Figure 2) [28]. The acoustic treatment of the grids has three main effects. On the one hand, it induces a reduction in noise levels for frequencies lower than ≈ 3500 Hz when compared to the clean case, eliminating the two tonal peaks observed for the finest grid, i.e., grid A. On the other, broad ‘humps’ with narrower peaks appear in the range $5000 \text{ Hz} \leq f \leq 15000 \text{ Hz}$, producing large noise increases when compared to the untreated case. Figure 15 better illustrates this point (the frequency f is here converted to the non-dimensional form of Strouhal number $St = fd/U_\infty$, see discussion in III.B.2). Figure 18 in particular reveals that the sixth-power velocity scaling produces a particularly good collapse for the self-noise of the untreated grids, with the only exception of the tonal peaks seen in the spectra of the finest grid (grid A), suggesting a different aeroacoustic origin than the broadband counterpart.

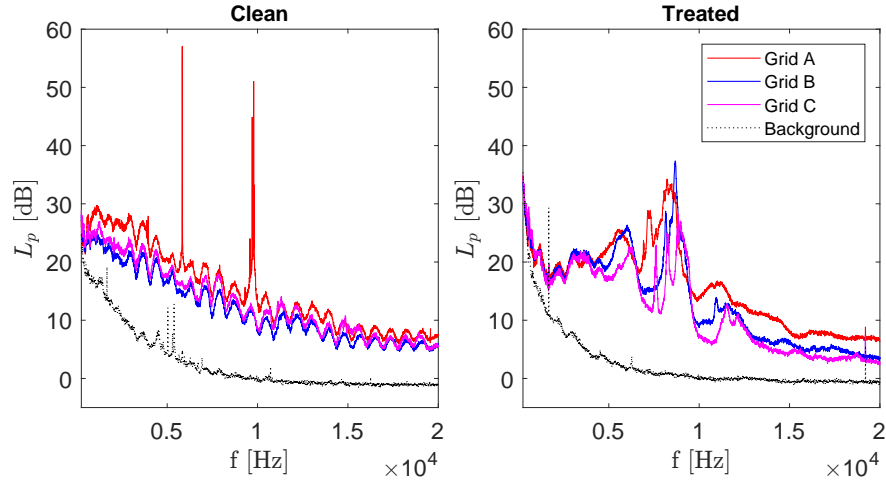


Fig. 14 Comparison of sound pressure level L_p spectra produced by different grids for both the clean and acoustically-treated cases for $U_\infty = 30$ m/s as recorded by a microphone at $\vartheta = 50^\circ$ (scheme in Figure 3, right). Frequency resolution $\Delta f = 5$ Hz.

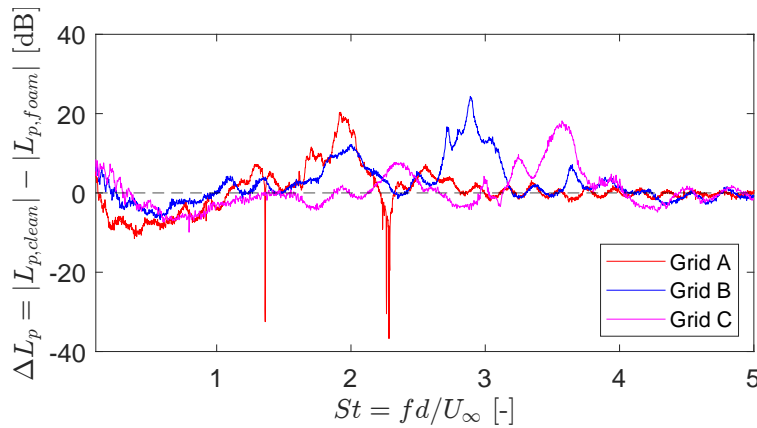


Fig. 15 Difference of sound pressure level L_p produced by clean and acoustically-treated grids for $U_\infty = 30$ m/s as recorded by a microphone at $\vartheta = 50^\circ$ (scheme in Figure 3, right). Frequency resolution $\Delta f = 5$ Hz ($\Delta St \approx 0.0015$).

2. Velocity scaling

The alternating peaks and troughs occurring at constant frequencies and caused by the acoustic reflections in the clean configuration are evident. The strong narrowband tones are also clearly visible for the finest grid A. The amplitude of such tones is dependent on the inflow velocity while their frequency is only weakly affected by it. The contour plots for the treated grids (Fig. 17) highlight instead the presence of the broad ‘humps’ observed in Figs. 13 and 14 whose centre frequencies seem to linearly increase with the inflow velocity. Such a trend suggests a non-dimensionalization of the frequency in the form of a Strouhal number $St = fd/U_\infty$, typical of noise sources deriving from the interaction of a flow with a solid surface [36]. Following Zamponi *et al.* [37], Figures 18 and 19 report the sound pressure level spectrum of both clean and acoustically-treated grids scaled by the sixth power of the inflow velocity U_∞ , with the frequency substituted by the Strouhal number $St = fd/U_\infty$. Such scaling is to be expected for compact solid surfaces interacting with low Mach number flows [38]. Figs. 16 and 17 show the contour plots of the sound pressure level spectra L_p for all grid configurations and all tested inflow velocities at the same microphone position as in III.B.1 ($\vartheta = 50^\circ$, see Fig. 3, right).

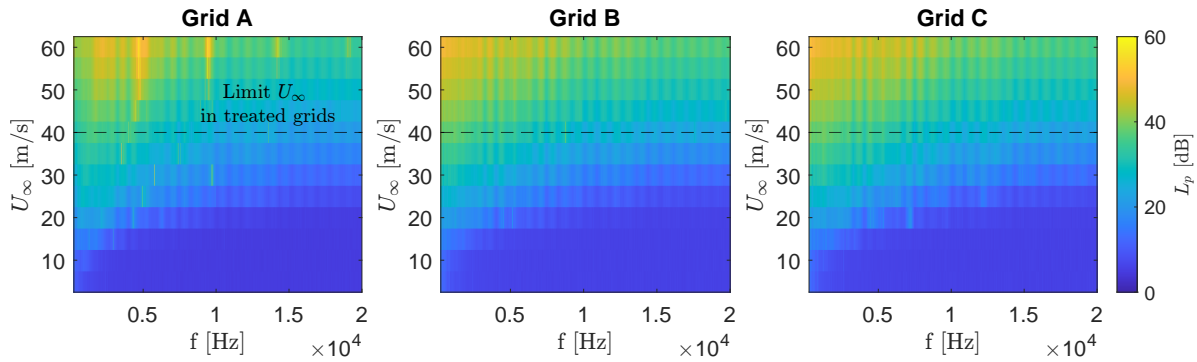


Fig. 16 Sound pressure level L_p spectra contour plots produced by the three different clean grids for varying U_∞ as recorded by a microphone at $\vartheta = 50^\circ$ (scheme in Figure 3, right). Frequency resolution $\Delta f = 5$ Hz.

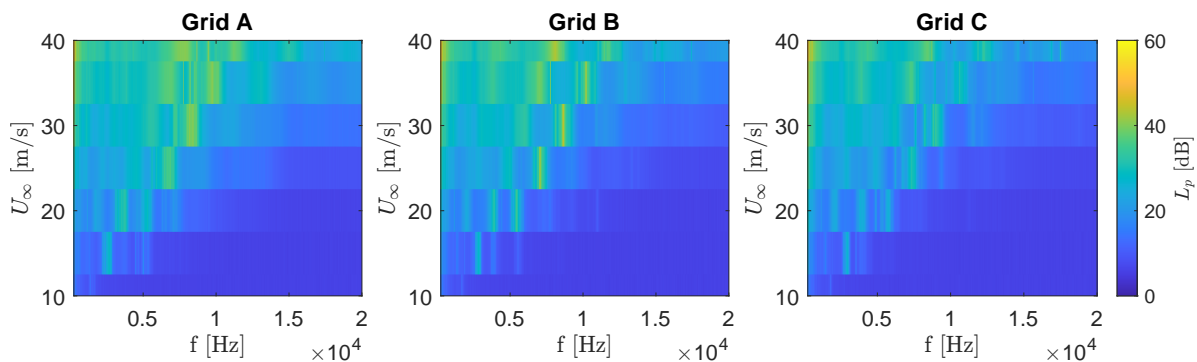


Fig. 17 Sound pressure level L_p spectra contour plots produced by the three different acoustically-treated grids for varying U_∞ as recorded by a microphone at $\vartheta = 50^\circ$ (scheme in Figure 3, right). Frequency resolution $\Delta f = 5$ Hz.

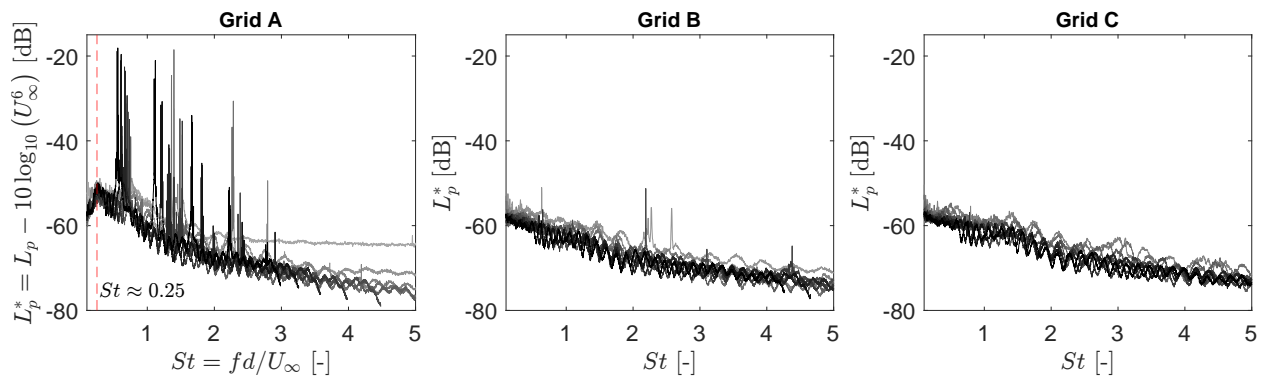


Fig. 18 Scaled sound pressure level L_p^* spectrum produced by the three different grids with no acoustic treatment for varying U_∞ as recorded by a microphone at $\vartheta = 50^\circ$ (scheme in Figure 3, right). Larger U_∞ values are indicated through darker lines. Frequency resolution $\Delta f = 5$ Hz ($\Delta St \approx 0.0015$).

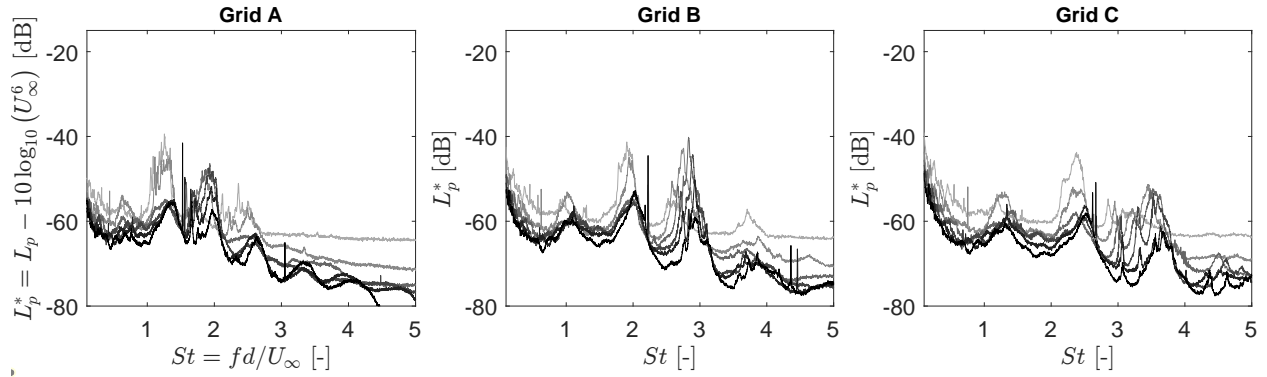


Fig. 19 Scaled sound pressure level L_p^* spectrum produced by the three different grids with acoustic treatment for varying U_∞ as recorded by a microphone at $\vartheta = 50^\circ$ (scheme in Figure 3, right). Larger U_∞ values are indicated through darker lines. Frequency resolution $\Delta f = 5$ Hz ($\Delta St \approx 0.0015$).

Furthermore, this grid is the only (not acoustically-treated) one displaying a broad peak centred at $St \approx 0.25$. Such value is within the typical Strouhal number range of vortex shedding phenomena for slender cylinders (of either circular or rectangular cross sections) [39]. On the other hand, all acoustically-treated grids show the presence of broad ‘humps’ at roughly constant Strouhal numbers and the velocity scaling in this case is not as effective as for the ‘clean’ grids (Figure 19). To illustrate this point, Figure 20 reports the 1/12-octave band sound pressure level $L_{p,1/12}$ for increasing inflow velocities at centre frequencies corresponding to the Strouhal numbers $St_c = 1, 2$ and 3 for both the clean and acoustically-treated intermediate grid (grid B). Such values coincide with the centre Strouhal numbers of the three broad humps observable in Figure 19, centre plot. The inflow velocity U_∞ has been substituted by the bar Reynolds number $Re_d = U_\infty d / \nu$, deemed a more representative parameter [40]. The velocity power-law in the case of the untreated case is evident at all three Strouhal numbers for $Re_d > 15000$ (deviations at lower Re_d could be due to lower signal-to-noise ratios). The treated grid instead shows evidence of a clear sixth-power law relationship with the inflow velocity only at the lowest Strouhal number considered ($St_c = 1$).

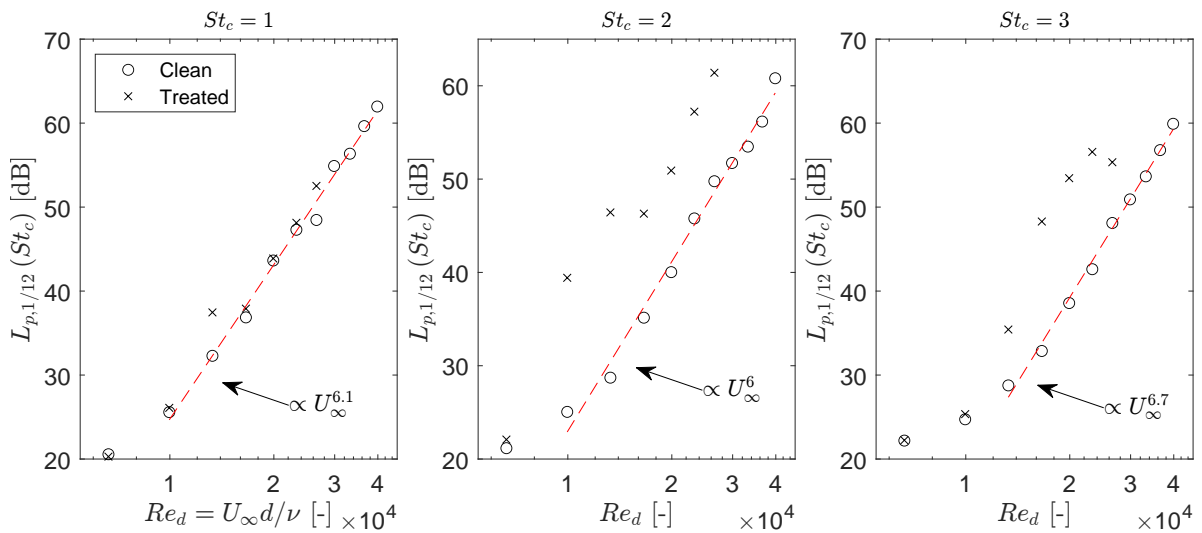


Fig. 20 Trend of sound pressure level of 1/12-octave band for increasing Reynolds numbers for the intermediate grid B. The 1/12-octave band centre frequency corresponds to the Strouhal number ($St_c = f_c d / U_\infty$) above each plot. The fitting power-law curve corresponds to the untreated case only.

3. Source directivity

Determining the radiation pattern of the system composed of the grids and the axisymmetric nozzle can be useful in evaluating the effects of adding an acoustic treatment to the grids. Figure 21 reports the overall A-weighted sound pressure level (OASPL) in the frequency range $250 \text{ Hz} \leq f \leq 20000 \text{ Hz}$ for all grid configurations for $U_\infty = 30 \text{ m/s}$. A few remarks can be made. First of all, the shielding effect of the nozzle and the inherently dipolar character of the aerodynamic noise generated by the grids are clearly visible in the cardioid-like shape of the directivity pattern for all grids, independently of the acoustic treatment. Secondly, the benefits of the acoustic treatment are particularly clear for the case of the finest grid (grid A), reaching OASPL reductions up to 8 dBA in certain emission angles. This can be easily explained by the fact that the application of melamine foam effectively prevents the development of the strong tonal peaks observed in the untreated case. For the case of the intermediate grid (grid B) instead, the acoustic treatment leads to a slight increment of the noise emissions of up to 3 dBA towards the higher end of the polar angles considered in this study. Finally, the coarsest grid (grid C) shows a slight decrease in noise emissions up to 3 dBA towards the lower end of the same polar range when acoustically-treated. Further information can be obtained if the radiation pattern is evaluated for the sound pressure level over specific frequency bands.

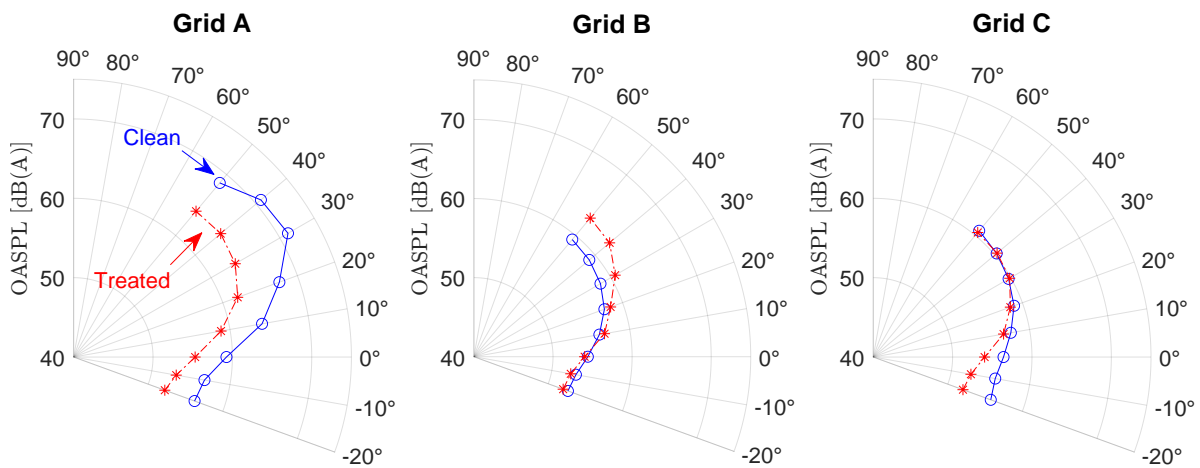


Fig. 21 Overall A-weighted sound pressure level (OASPL) radiation pattern for all tested configurations for $U_\infty = 30 \text{ m/s}$.

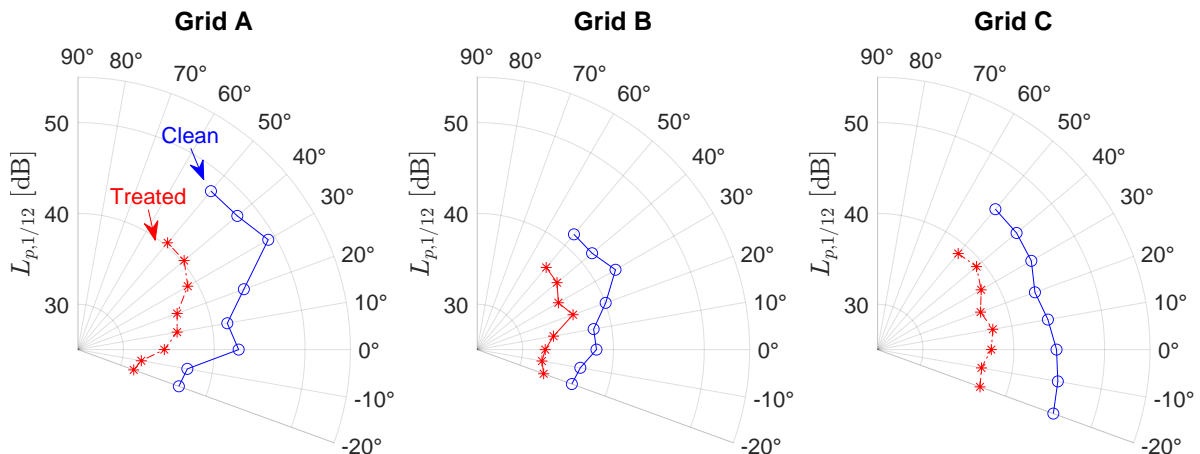


Fig. 22 Radiation pattern of sound pressure level of 1/12-octave band with centre frequency corresponding to a Strouhal number $St_c = f_c d / U_\infty = 0.5$ for all tested configurations ($U_\infty = 30 \text{ m/s}$).

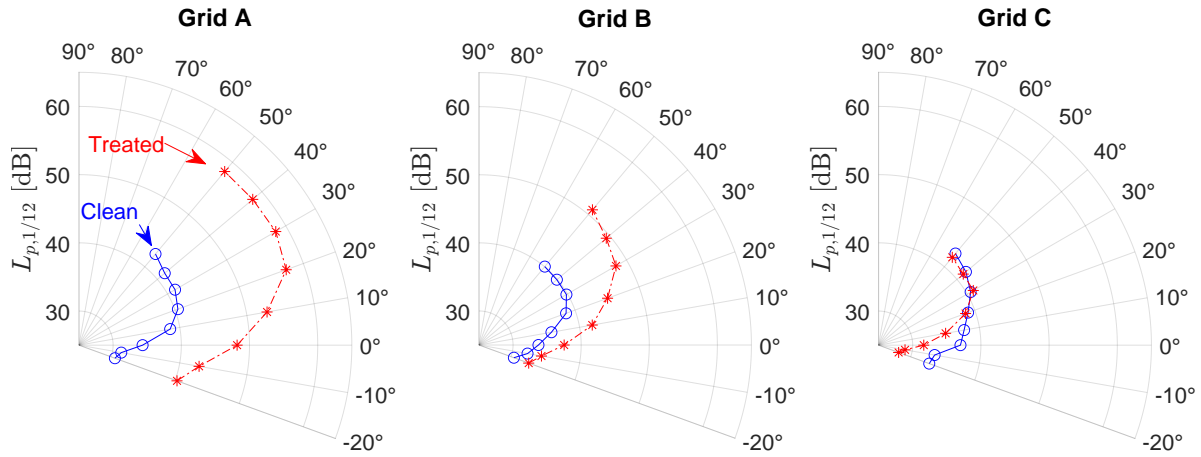


Fig. 23 Radiation pattern of sound pressure level of 1/12-octave band with centre frequency corresponding to a Strouhal number $St_c = f_c d / U_\infty = 2$ for all tested configurations ($U_\infty = 30$ m/s).

Figures 22 and 23 show the 1/12-octave band sound pressure level $L_{p,1/12}$ radiation patterns for all tested configurations and for centre frequencies corresponding to $St_c = 0.5$ and 2. The former is representative of the Strouhal number range for which the acoustic treatment seemed the most effective at $\vartheta = 50^\circ$ for the intermediate grid B, see Fig. 15. The second ($St_c = 2$) is instead deemed representative as it roughly corresponds to the centre Strouhal number of the two ‘humps’ seen in the spectra of grids A and B (the ones of grid C being shifted to higher values of St). It is clear that the trends observed for the microphone at $\vartheta = 50^\circ$ remain valid for the other positions along the microphone directivity arc. This confirms the effectiveness of the grid treatments at reducing noise emissions for lower Strouhal numbers ($St_c \leq 1$ in this case) and the introduction of additional noise in isolated broad ‘humps’ centred at specific Strouhal numbers.

IV. Conclusions

A set of square-mesh and square-bar grids of constant porosity and varying mesh dimensions placed upstream of an axisymmetric contraction were the subject of two experimental campaigns focusing on both their turbulence production and self-noise characteristics. The addition of a melamine foam coating on the downstream side of the grids was investigated as a potential mitigation strategy for the grids’ self-noise. The main conclusions of this study are:

- the acoustic treatment leads to a slight reduction in the streamwise turbulence intensity ($\approx 5\%$) and to a more substantial reduction in the longitudinal integral length scale ($\approx 25\%$) with respect to the untreated case;
- the spectral distribution of the streamwise velocity fluctuations is not affected by the melamine foam coating and is well captured by the von Kármán semi-empirical model for homogeneous and isotropic turbulence;
- the acoustic treatment is an effective solution for the suppression of strong tonal peaks in the acoustic far-field emissions. Furthermore, it allows for a general decrease in the broadband noise component for Strouhal numbers lower than unity;
- additional noise, on the other hand, is caused by the treatment in the form of broad ‘humps’ in the spectra at roughly constant Strouhal numbers.

In conclusion, the effectiveness of the acoustic treatment of the downstream surface of turbulence-producing grids seems to be dependent on the frequency range of interest in the intended application. A study focusing on the use of different coating materials and/or different foam thicknesses would be helpful in further understanding the potential of this mitigation strategy. The benefits of dampening the acoustic reflections coming from noise sources placed outside of the wind tunnel’s nozzle were not considered in this study. This could provide additional reasons for the application of such a type of treatment to turbulence grids in open-jet wind tunnels.

Funding Sources

This work is part of the HOPE (Hydrogen Optimized multi-fuel Propulsion system for clean and silEnt aircraft) project, and has received funding from the European Union’s Horizon Europe research and innovation programme under grant

agreement No. 101096275. Additionally, this publication is also a part of the *Listen to the future* project (project number 20247), a part of the Veni 2022 research programme (Domain Applied and Engineering Sciences). The latter project is granted to Roberto Merino-Martinez and is (partially) financed by the Dutch Research Council (NWO).

References

- [1] Leylekian, L., Covrig, A., and Maximova, A. (eds.), *Aviation Noise Impact Management: Technologies, Regulations, and Societal Well-being in Europe*, Springer International Publishing, Cham, 2022. <https://doi.org/10.1007/978-3-030-91194-2>.
- [2] Aalmoes, R., Tojal Castro, M., Sieben, N., and Roosien, R., “Drone noise in my backyard: the challenges for public acceptability,” *INTER-NOISE and NOISE-CON Congress and Conference Proceedings*, Vol. 265, No. 3, 2023, pp. 4987–4993. https://doi.org/10.3397/IN_2022_0721.
- [3] Sijtsma, P., “Phased Array Beamforming Applied to Wind Tunnel And Fly-Over Tests,” Tech. Rep. NLR-TP-2010-549, National Aerospace Laboratory NLR, Dec. 2010.
- [4] Merino-Martínez, R., Sijtsma, P., Snellen, M., Ahlefeldt, T., Antoni, J., Bahr, C. J., Blacodon, D., Ernst, D., Finez, A., Funke, S., Geyer, T. F., Haxter, S., Herold, G., Huang, X., Humphreys, W. M., Leclère, Q., Malgoezar, A., Michel, U., Padois, T., Pereira, A., Picard, C., Sarradj, E., Siller, H., Simons, D. G., and Spehr, C., “A review of acoustic imaging methods using phased microphone arrays: Part of the “Aircraft Noise Generation and Assessment” Special Issue,” *CEAS Aeronautical Journal*, Vol. 10, No. 1, 2019, pp. 197–230. <https://doi.org/10.1007/s13272-019-00383-4>.
- [5] Ramos-Romero, C., Green, N., Torija, A. J., and Asensio, C., “On-field noise measurements and acoustic characterisation of multi-rotor small unmanned aerial systems,” *Aerospace Science and Technology*, Vol. 141, 2023, p. 108537. <https://doi.org/10.1016/j.ast.2023.108537>.
- [6] Allen, C. S., Blake, W. K., Dougherty, R. P., Lynch, D., Soderman, P. T., and Underbrink, J. R., *Aeroacoustic Measurements*, Springer Berlin Heidelberg, Berlin, Heidelberg, 2002. <https://doi.org/10.1007/978-3-662-05058-3>.
- [7] VanDercreek, C. P., Merino-Martinez, R., Sijtsma, P., and Snellen, M., “Evaluation of the effect of microphone cavity geometries on acoustic imaging in wind tunnels,” *Applied Acoustics*, Vol. 181, No. 108154, 2021, pp. 1–15. <https://doi.org/10.1016/j.apacoust.2021.108154>.
- [8] Chong, T., Joseph, P., and Davies, P., “Design and performance of an open jet wind tunnel for aero-acoustic measurement,” *Applied Acoustics*, Vol. 70, No. 4, 2009, pp. 605–614. <https://doi.org/10.1016/j.apacoust.2008.06.011>.
- [9] Mayer, Y. D., Jawahar, H. K., Szóke, M., Ali, S. A. S., and Azarpeyvand, M., “Design and performance of an aeroacoustic wind tunnel facility at the University of Bristol,” *Applied Acoustics*, Vol. 155, 2019, pp. 358–370. <https://doi.org/10.1016/j.apacoust.2019.06.005>.
- [10] Okoronkwo, M., Alsaif, R., Haklander, R., Baba, S., Eburn, J., Lu, Z., Arafa, N., Stalnov, O., Ekmekci, A., and Lavoie, P., “Design and characterization of the university of Toronto hybrid anechoic wind tunnel,” *Applied Acoustics*, Vol. 228, 2025, p. 110294. <https://doi.org/10.1016/j.apacoust.2024.110294>.
- [11] Barahona, M., Weijer, T. A. F. V., Rius-Vidales, A. F., and Kotsonis, M., “Stability of Swept Wing Boundary Layers under Non-Adiabatic Wall Conditions,” *AIAA SCITECH 2024 Forum*, American Institute of Aeronautics and Astronautics, Orlando, FL, 2024. <https://doi.org/10.2514/6.2024-0695>.
- [12] Lighthill, M. J., “On sound generated aerodynamically II. Turbulence as a source of sound,” *Proceedings of the Royal Society of London. Series A. Mathematical and Physical Sciences*, Vol. 222, No. 1148, 1954, pp. 1–32. <https://doi.org/10.1098/rspa.1954.0049>.
- [13] Amiet, R., “Acoustic radiation from an airfoil in a turbulent stream,” *Journal of Sound and Vibration*, Vol. 41, No. 4, 1975, pp. 407–420. [https://doi.org/10.1016/S0022-460X\(75\)80105-2](https://doi.org/10.1016/S0022-460X(75)80105-2).
- [14] Hanson, L. P., Zang, B., and Azarpeyvand, M., “Experimental Characterisation of Cylinder-Induced Turbulence Ingestion in Propellers Operating in Edgewise Flight,” *30th AIAA/CEAS Aeroacoustics Conference (2024)*, American Institute of Aeronautics and Astronautics, Rome, Italy, 2024. <https://doi.org/10.2514/6.2024-3100>.
- [15] Van Arnhem, N., De Vries, R., Sinnige, T., Vos, R., Eitelberg, G., and Veldhuis, L. L. M., “Engineering Method to Estimate the Blade Loading of Propellers in Nonuniform Flow,” *AIAA Journal*, Vol. 58, No. 12, 2020, pp. 5332–5346. <https://doi.org/10.2514/1.J059485>.

- [16] Comte-Bellot, G., and Corrsin, S., "The use of a contraction to improve the isotropy of grid-generated turbulence," *Journal of Fluid Mechanics*, Vol. 25, No. 4, 1966, pp. 657–682. <https://doi.org/10.1017/S0022112066000338>.
- [17] Roach, P., "The generation of nearly isotropic turbulence by means of grids," *International Journal of Heat and Fluid Flow*, Vol. 8, No. 2, 1987, pp. 82–92. [https://doi.org/10.1016/0142-727X\(87\)90001-4](https://doi.org/10.1016/0142-727X(87)90001-4).
- [18] Kurian, T., and Fransson, J. H. M., "Grid-generated turbulence revisited," *Fluid Dynamics Research*, Vol. 41, No. 2, 2009, p. 021403. <https://doi.org/10.1088/0169-5983/41/2/021403>.
- [19] Geyer, T. F., Poppe, W., and Sarradj, E., "Measurement of flow noise generation and pressure loss of nets and screens," *Applied Acoustics*, Vol. 134, 2018, pp. 69–74. <https://doi.org/10.1016/j.apacoust.2018.01.008>.
- [20] Bowen, L., Celik, A., Azarpeyvand, M., and Da Silva, C. R. I., "Grid Generated Turbulence for Aeroacoustic Facility," *AIAA Journal*, Vol. 60, No. 3, 2022, pp. 1833–1847. <https://doi.org/10.2514/1.J060851>.
- [21] Wojno, J. P., Mueller, T. J., and Blake, W. K., "Turbulence Ingestion Noise, Part 1: Experimental Characterization of Grid-Generated Turbulence," *AIAA Journal*, Vol. 40, No. 1, 2002, pp. 16–25. <https://doi.org/10.2514/2.1636>.
- [22] Wojno, J. P., Mueller, T. J., and Blake, W. K., "Turbulence Ingestion Noise, Part 2: Rotor Aeroacoustic Response to Grid-Generated Turbulence," *AIAA Journal*, Vol. 40, No. 1, 2002, pp. 26–32. <https://doi.org/10.2514/2.1637>.
- [23] Li, L., Zhu, H., Maryami, R., Zhang, X., and Liu, Y., "Flow and acoustic characterization of turbulence grids at wind tunnel nozzle exit," *Journal of Sound and Vibration*, Vol. 590, 2024, p. 118535. <https://doi.org/10.1016/j.jsv.2024.118535>.
- [24] Bereketab, S., Wang, H. W., Mish, P., and Devenport, W. J., "The Surface Pressure Response of a NACA 0015 Airfoil Immersed in Grid Turbulence: Characteristics of the Turbulence - Volume 1," NASA technical report, Virginia Tech, Nov. 2000.
- [25] Hutcheson, F., Brooks, T., Burley, C., and Stead, D., "Measurement of the Noise Resulting from the Interaction of Turbulence with a Lifting Surface," *17th AIAA/CEAS Aeroacoustics Conference (32nd AIAA Aeroacoustics Conference)*, American Institute of Aeronautics and Astronautics, Portland, Oregon, 2011. <https://doi.org/10.2514/6.2011-2907>.
- [26] Merino-Martínez, R., Rubio Carpio, A., Lima Pereira, L. T., Van Herk, S., Avallone, F., Ragni, D., and Kotsonis, M., "Aeroacoustic design and characterization of the 3D-printed, open-jet, anechoic wind tunnel of Delft University of Technology," *Applied Acoustics*, Vol. 170, 2020, p. 107504. <https://doi.org/10.1016/j.apacoust.2020.107504>.
- [27] Quaroni, L. N., Merino-Martínez, R., Monteiro, F. D., and Kumar, S. S., "Collective blade pitch angle effect on grid turbulence ingestion noise by an isolated propeller," *30th AIAA/CEAS Aeroacoustics Conference (2024)*, American Institute of Aeronautics and Astronautics, Rome, Italy, 2024. <https://doi.org/10.2514/6.2024-3209>.
- [28] Quaroni, L., and Merino-Martínez, R., "Mitigation strategies for acoustic reflections generated by an axisymmetric wind tunnel nozzle," *11th Forum Acusticum Euronoise Conference, June 23 – 26 2025, Málaga, Spain, 2025*.
- [29] Quaroni, L. N., Sinnige, T., and Merino-Martínez, R., "Investigation of noise generation by a model-propeller in turbulent inflow through advanced signal processing techniques (submitted)," *2025 AIAA AVIATION Forum*, Las Vegas, USA, 2024.
- [30] Jorgensen, F. E., "How to measure turbulence with hot-wire anemometers: a practical guide," , 2005.
- [31] Go, S. T., Kingan, M. J., Bowen, L., and Azarpeyvand, M., "Noise of a shrouded propeller due to ingestion of grid-generated turbulence," *Journal of Sound and Vibration*, 2023, p. 118044. <https://doi.org/10.1016/j.jsv.2023.118044>.
- [32] Pope, S. B., *Turbulent flows*, 1st ed., Cambridge Univ. Press, Cambridge, 2015.
- [33] Isaza, J., Salazar, R., and Warhaft, Z., "On grid-generated turbulence in the near- and far field regions," *Journal of Fluid Mechanics*, Vol. 753, 2014, pp. 402–426. <https://doi.org/10.1017/jfm.2014.375>.
- [34] Von Kármán, T., "Progress in the Statistical Theory of Turbulence," *Proceedings of the National Academy of Sciences*, Vol. 34, No. 11, 1948, pp. 530–539. <https://doi.org/10.1073/pnas.34.11.530>.
- [35] Devenport, W. J., Staubs, J. K., and Glegg, S. A., "Sound radiation from real airfoils in turbulence," *Journal of Sound and Vibration*, Vol. 329, No. 17, 2010, pp. 3470–3483. <https://doi.org/10.1016/j.jsv.2010.02.022>.
- [36] Blake, W. K., *Mechanics of Flow-Induced Sound and Vibration*, second edition ed., Academic Press, London, 2017.
- [37] Zamponi, R., Avallone, F., Ragni, D., and Van Der Zwaag, S., "On the Aerodynamic-Noise Sources in a Circular Cylinder Coated with Porous Materials," *28th AIAA/CEAS Aeroacoustics 2022 Conference*, American Institute of Aeronautics and Astronautics, Southampton, UK, 2022. <https://doi.org/10.2514/6.2022-3042>.

- [38] Curle, N., “The influence of solid boundaries upon aerodynamic sound,” *Proceedings of the Royal Society of London. Series A. Mathematical and Physical Sciences*, Vol. 231, No. 1187, 1955, pp. 505–514. <https://doi.org/10.1098/rspa.1955.0191>.
- [39] Octavianty, R., Asai, M., and Inasawa, A., “Experimental Study on Vortex Shedding and Sound Radiation from a Rectangular Cylinder at Low Mach Numbers,” *TRANSACTIONS OF THE JAPAN SOCIETY FOR AERONAUTICAL AND SPACE SCIENCES*, Vol. 59, No. 5, 2016, pp. 261–268. <https://doi.org/10.2322/tjsass.59.261>.
- [40] Margnat, F., Gonçalves Da Silva Pinto, W. J., and Noûs, C., “Cylinder aeroacoustics: experimental study of the influence of cross-section shape on spanwise coherence length,” *Acta Acustica*, Vol. 7, 2023, p. 4. <https://doi.org/10.1051/aacus/2022061>.